Hierarchical crack patterns of metal films sputter deposited on soft elastic substrates

Senjiang Yu [1,*,†] Long Ma,[2,*] Linghui He,[2] and Yong Ni[2,‡]

[1]*College of Materials and Environmental Engineering, Hangzhou Dianzi University, Hangzhou 310018, People's Republic of China*
[2]*CAS Key Laboratory of Mechanical Behavior and Design of Materials, Department of Modern Mechanics, University of Science and Technology of China, Hefei, Anhui 230026, People's Republic of China*

(Received 24 June 2019; published 19 November 2019)

Controlled cracks are useful in a wide range of applications, including stretchable electronics, microfluidics, sensors, templates, biomimics, and surface engineering. Here we report on the spontaneous formation of hierarchical crack patterns in metal (nickel) films sputter deposited on soft elastic polydimethylsiloxane (PDMS) substrates. The experiment shows that the nickel film generates a high tensile stress during deposition, which is relieved by the formation of disordered crack networks (called primary cracks). Due to the strong interfacial adhesion and soft substrate, the cracks can penetrate into the PDMS substrate deeply. The width and depth of the primary cracks both increase with increasing film thickness, whereas the crack spacing is insensitive to the film thickness. The film pieces dividing by the primary cracks can fracture further when they are triggered by an external disturbance due to the residual tensile stress, resulting in the formation of fine crack networks (called secondary cracks). The width and spacing of the secondary cracks show different behaviors in comparison to the primary cracks. The morphological characteristics, growth behaviors, and formation mechanisms of the primary and secondary cracking modes have been discussed in detail. The report in this work could provide better understanding of two distinct cracking modes with different sizes and morphologies.

DOI: 10.1103/PhysRevE.100.052804

I. INTRODUCTION

Fracture patterns can be widely observed in natural systems, including geological structures, rocks, drying mud, and biological tissues [1–3]. They are also very common in artificial systems such as aged paints, coatings, films, and 2D materials [4–6]. Although fractures are usually troublesome in the fabrication and usage of functional devices, recent studies also showed that controlled cracks can be beneficial for a variety of technical applications including micro/nanofluidic devices [7,8], stretchable transistors [9], conducting electrodes [10,11], pressure sensors [12,13], selective surface adsorption [14], controlled wettability [15], biological assays [16], etc. The controllable formation of various crack arrays is intrinsic and necessary to attain specified goals (or use in different fields). For examples, the crack-assisted lithography needs cracks with completely controlled propagation paths, which can be regulated by prefabrication of notch structures (for crack initiation) and free boundaries (for crack termination) [8,17]. The crack-based microfluidics requires unidirectional cracks (no strict requirement for crack period and propagation path), which can be conveniently fabricated and tuned by uniaxial stretching and releasing [7,8]. Both regular and random crack arrays can be used as crack-based ultrasensitive sensors [12,13]. Only randomly oriented crack arrays are needed for crack-assisted templates (e.g., fabrication of transparent conducting electrodes) to minimize the Moiré effect problem and decrease the fabrication cost [10,11].

Although the basic understanding of an isolated crack propagation has been captured by a fracture mechanics approach, formation of fascinating patterns with appearance of multiple cracks, i.e., wavy [18], spiral [19], starlike [20], *en passant* [21], and so on, is still a challenging problem even in 2D cases due to complex crack interactions. The rich variety of crack patterns is more frequently generated in film-substrate systems under residual tensile stress or mechanical loading since it could be also influenced by mechanical property of the substrate and the interface property between film and substrate. There exist three distinct crack modes in the film-substrate systems including cracks within the film, cracks penetrating into the substrate, and cracks with interface debonding [22–24]. For weak interfacial adhesion strength, the cracks are susceptible to deflect into the interface, leading to interface debonding or delamination [25,26]. If the fracture toughness of film is much smaller than that of substrate, then the cracks are usually limited within the film. The so-called mud crack patterns observed in drying thin layers [27–30] or in amorphous Si thin film electrodes during electrochemical cycling [31] belong to this film cracking scenario.

Understanding characteristic size and hierarchy of these crack patterns has been greatly improved [32–47]. Hexagonal crack pattern can be viewed as a result of maximizing the total energy releasing rate [35]. Anisotropic crack pattern can be induced by directional drying [37]. There is temporal hierarchy of crack patterns that depends on the cracking history since the existing cracks regulate the elastic stress field that governs formation of future cracks [32–34]. Selection rule of ring or radial crack patterns observed in brittle coatings

*These authors contributed equally to this work.
†senjiangyu@hotmail.com
‡yni@ustc.edu.cn

 ©2019 American Physical Society

due to indentation has been established in a fracture mode map in terms of two dimensionless parameters [36]. For the characteristic size of these crack patterns, a common feature is that it increases with increasing the film thickness as a power-law of 2/3 or 1 [38–47]. When the delamination occurs at the interface the power-law is 1, which can be understood by a shear-lag analysis [39,40] or the concept of maximizing energy release rate [26,41]. When the delamination is limited, the power-law is 2/3, which can be explained as the result of compromise between the energy cost of creating new surfaces and the elastic energy released during cracking [42–46]. Interestingly, if the fracture toughness of substrate is not very high or crystallographic substrates are applied, then the cracks tend to penetrate into the substrate under high tensile stress. It has been reported that the cracks in brittle films (Si_3N_4, silica, or manganite) can penetrate into crystallized substrates (Si or scandate), leading to periodically oscillating crack paths along specific orientations [17,48–50]. When a buffer layer (SiO_2) was intercalated into the interface between the film and substrate, the cracks will terminate at the buffer layer surface and the crack orientation vanishes [17,50]. The cracks penetrating into the substrate are also frequently observed in brittle films on ductile and compliant substrates such as brass, polyethylene terephthalate (PET) and polydimethylsiloxane (PDMS) [51–53].

Although various cracking phenomena in metal and inorganic films on compliant substrates have been documented in the previous literature [4,51–54], the understanding for initiation, evolution, and thus control of the cracks (especially those penetrating into the substrate) is still insufficient up to now. In this work, we report on the spontaneous formation of hierarchical crack patterns in nickel films sputter deposited on soft PDMS substrates. Two distinct cracking modes with different morphologies and formation mechanisms, namely primary and secondary cracks, are observed in the experiment. The primary cracks are caused by the high tensile stress in the film during the sputtering process and they can penetrate into the PDMS substrate deeply. Their width and depth increase with increasing film thickness, while the number density is almost unchanged during deposition. The secondary cracks triggered by an external disturbance rarely penetrate into the substrate, and the crack width is inversely proportional to the crack number density. The results provide the ability to generate controlled crack morphologies via regulating the film thickness and mechanical loading.

II. EXPERIMENTAL DETAILS

A. Substrate preparation

Polydimethylsiloxane (PDMS, Dow Corning's Sylgard 184) was adopted as soft elastic substrates in this study. The gel and cross-linker were mixed with 10:1 weight ratio. After degassing in a low-pressure chamber, the liquid PDMS was spin-coated onto clean glass slides with about $10 \times 10\,\mathrm{mm}^2$ in size. The rotation speed and time were fixed at 3500 rpm (revolutions per minute) and 30 s, respectively. Then the substrates were placed onto a hot plate with 80 °C for more than 3 hours, resulting in the transition from liquid PDMS to solid PDMS. The thickness of the solidified PDMS layer was about 22 μm. The elastic modulus of PDMS (upon compression) was about 2.7 MPa measuring by a material testing machine (Instron 3367). The vacuum condition and heating treatment (below 150 °C) have no obvious influence on the optical and mechanical properties of the PDMS.

B. Film fabrication

The films were prepared by using direct current magnetron sputtering at room temperature. The sputtering target was a piece of nickel disk with the purity of 99.9%, the diameter of 60 mm and the thickness of 3 mm. Before sputtering, the gas pressure of the vacuum chamber was pumped below 2×10^{-4} Pa. Then the pure argon gas was filled into the chamber with the fixed pressure of 0.5 Pa. During sputtering, the electric current and voltage were about 0.2 A and 280 V, corresponding to a sputtering power of 56 W. The deposition rate of the film was calibrated to be about 0.25 nm/s. The deposition time was controlled by a computer and was ranged from 10 s to 20 min in this study. The elastic modulus of metal nickel (material parameter) was about 200 GPa, which was $\sim 10^5$ larger than that of PDMS.

C. Characterization

An optical microscopy (Olympus BX41) was used to investigate the surface morphologies of the films. A scanning electron microscopy (SEM, Zeiss Supra 55) was adopted to detect the details of the sample surface in the crack region. An atomic force microscopy (AFM, XE-100E, PSIA) was used to scan the 3D information of the crack patterns. A Vicker's diamond indenter (HXS-1000AY) was performed to investigate the influence of external loading on the crack morphology. The peak load P was varied from 0.1 to 10 N.

III. RESULTS AND DISCUSSION

A. Primary cracks

The typical surface morphologies of nickel (Ni) films sputter deposited on PDMS substrates with varied film thicknesses are shown in Fig. 1. The surface morphology of a thickness-gradient nickel film on the PDMS substrate can refer to Supplemental Material Fig. S1 [55]. When the film thickness is below a critical value (about 10 nm), the film surface is homogenous and rough under the optical microscope with small magnification, as shown in Fig. 1(a). In fact, the rough film surface is composed of labyrinth wrinkles resulting from isotropic residual compressive stress [see the inset of Fig. 1(a)]. The wrinkle wavelength increases obviously with increasing film thickness, as shown in Supplemental Material Fig. S2 [55]. The evolution of the wrinkling patterns in the thickness-gradient film can refer to our previous work [56]. The thickness-dependent wrinkling phenomenon is in agreement with many experimental observations [4,57–59] and theoretical prediction [59–61]. For a stressed film deposited on substrates, the energy releasing rate for a crack is proportional to the film thickness [22]. When the film thickness is beyond the critical value, cracks (namely primary cracks) start to form in the film, as shown in Fig. 1(b). The wrinkles are always perpendicular to the cracks due to the edge effect, as shown in Supplemental Material Fig. S3 [55]. The crack patterns become dominant while the surface

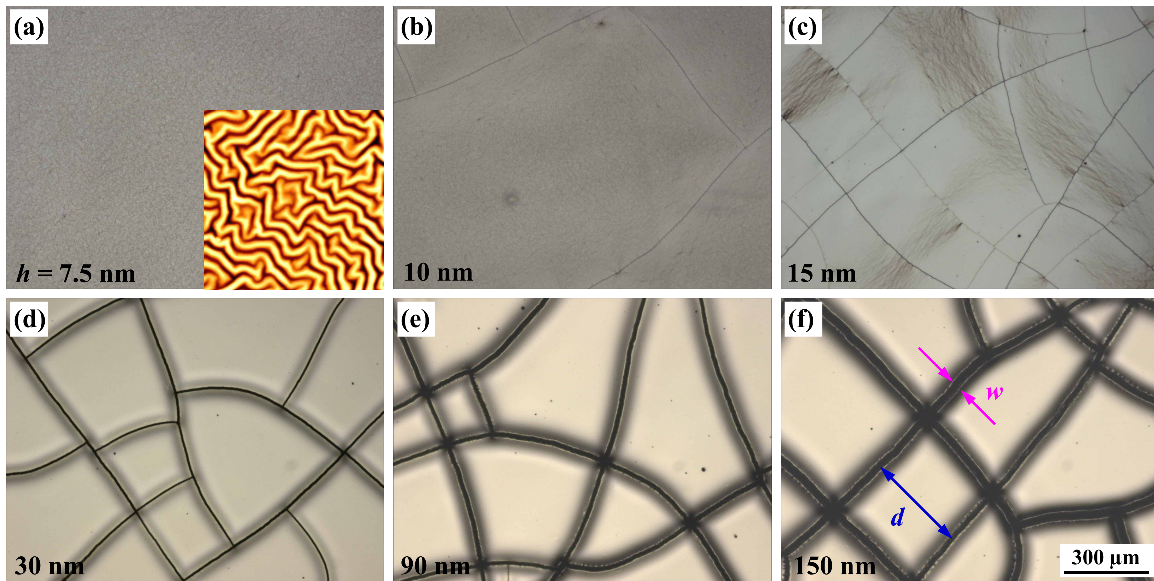

FIG. 1. Typical surface morphologies of Ni films sputter deposited on PDMS substrates with varied film thicknesses taken by the optical microscopy. (a) $h = 7.5$ nm; (b) $h = 10$ nm; (c) $h = 15$ nm; (d) $h = 30$ nm; (e) $h = 90$ nm; (f) $h = 150$ nm. Each image has a size of $1390 \times 1040\,\mu\text{m}^2$. The inset of (a) shows the enlarged atomic force microscopy (AFM) image with the size of $20 \times 20\,\mu\text{m}^2$. The spacing between neighboring cracks and the crack width are denoted as d and w, respectively.

wrinkles degenerate gradually with further increasing film thickness. The primary cracks are usually orthometric with each other and the intersection angles are almost equal to 90 degrees, similar to the disordered crack networks observed in drying mud, sol-gel films and plasma-treated PDMS surfaces [1,4,10,11,28,53].

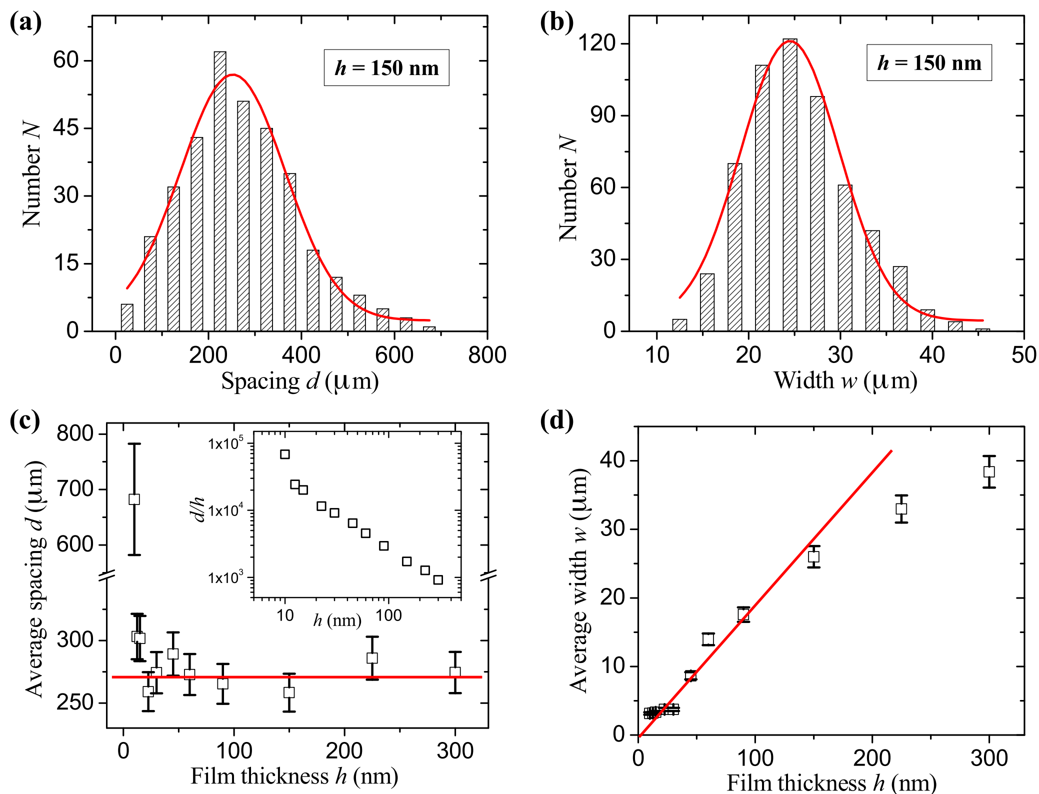

FIG. 2. (a), (b) Distributions of the spacing and width of primary cracks for the sample with $h = 150$ nm. The solid lines are fits to Gaussian distributions. (c) Dependence of the average crack spacing d on the film thickness h. The solid line represents an average value of $\sim 270\,\mu$m. The inset shows the relation between normalized crack spacing d/h and film thickness h. (d) Dependence of the average crack width w on the film thickness h. The solid line is a linear fit to the experimental data for smaller film thickness.

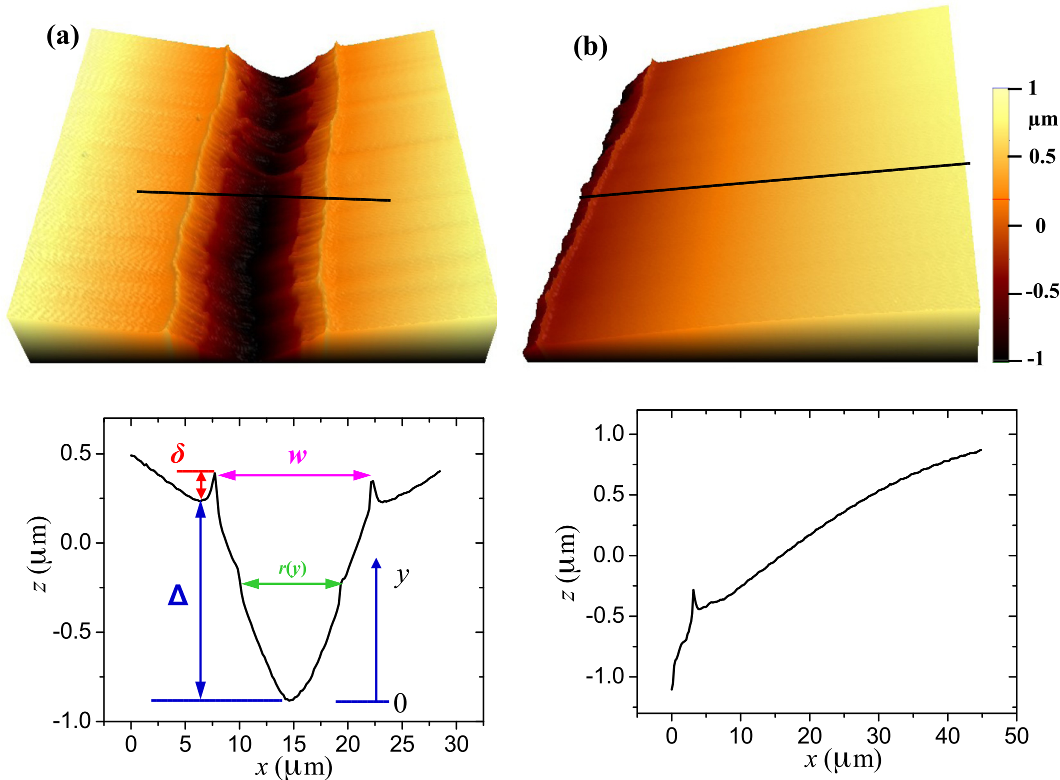

FIG. 3. Three-dimensional AFM images (top) and corresponding profiles (bottom) for the center (a) and side (b) of a primary crack. The depth of the crack and the lifting height at the crack edge are denoted as Δ and δ, respectively. Both AFM images have the sizes of $45 \times 45\ \mu\text{m}^2$. The scale bar can be applied to both images. $h = 60$ nm.

It should be noted here that the primary crack patterns in each sample are uniform. The optical micrographs of two samples with different film thicknesses are shown in Supplemental Material Figs. S4 and S5 [55]. We have measured a large number of spacing and width of primary cracks for each sample, as shown in Supplemental Material Figs. S6 and S7 [55]. Here the crack spacing is the distance between the two midpoints of opposite sides and the crack width is equivalent to fracture aperture. Figures 2(a) and 2(b) show the distributions of the spacing and width of primary cracks for the sample with $h = 150$ nm. The experimental data in each image fit well to a Gaussian distribution. Figures 2(c) and 2(d) show the dependences of the average spacing d and average width w on the film thickness h. We find that the crack spacing is almost unchanged when the film thickness is beyond 10 nm and its average value is about 270 μm. Near the critical point at which the primary cracks start to form, the crack spacing is much larger than the average value. On the other hand, the crack width increases approximately linearly with h for smaller film thickness. For large film thickness, however, the experimental data deviate from linearity gradually. Similar phenomenon that the crack width increases with the film thickness has also been observed in the drying colloidal systems and aged paintings [62].

To detect more structural details of the primary crack patterns, 3D images and corresponding profiles were taken by the AFM and the typical results are shown in Fig. 3. The AFM images and profiles for the primary crack in a thickness-gradient film can refer to Supplemental Material Fig. S8 [55]. The statistical results (including crack width, crack depth, etc.) for the primary crack in the thickness-gradient film are shown in Supplemental Material Fig. S9 [55]. We find that the crack profile is "V" shaped. Each edge of the crack has a peak due to the deformation of the soft substrate, in consistent with the previous studies [4,52,63,64]. The crack zone collapses obviously compared to other film surfaces, resulting in the formation of a neck of PDMS at the crack. It can be seen from Fig. 1 that there exist three different regions: a black central line, a bright thin line, and a shadow region on each side. The black central line corresponds to the primary crack, the bright thin line represents the peak at crack edge and the shadow region is attributed to the uneven film surface near the crack. As the magnifications of optical micrographs increase, the shadow regions become obscure and indistinguishable, as shown in Supplemental Material Fig. S10 [55]. To detect whether or not the film delaminates from the PDMS substrate near the crack, we have examined the cross-sectional profiles of the film-substrate system, as shown in Supplemental Material Figs. S11 and S12 [55]. All the experimental measurements including optical microscopy, AFM and SEM indicate that no obvious interfacial debonding occurs near the crack. The depth of the primary crack (of the order of 1 μm) is much larger than the film thickness (tens nanometers), indicating that the primary crack has penetrated into the PDMS substrate deeply [17,48–53].

Figure 4(a) shows the dependence of the crack depth Δ on the crack width w for varied film thicknesses. We find that the crack depth increases approximately linearly with the crack

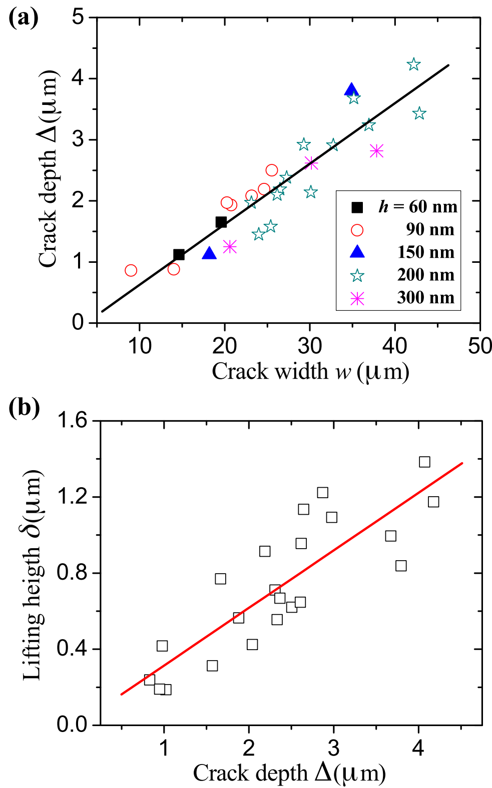

FIG. 4. (a) Dependence of the crack depth Δ on the crack width w for varied film thicknesses. (b) Dependence of the lifting height δ on the crack depth Δ. The solid lines are linear fits to the experimental data.

width, independent of the film thickness. This result indicates that the aspect ratio of the crack can keep constant when the crack size changes. Figure 4(b) shows the dependence of the lifting height δ at the crack edge on the crack depth Δ. The lifting height also increases approximately linearly with the crack depth. The film liftings at the two sides of crack are caused by the combined necking and the Poisson's ratio effects. After cracks form, the necked region causes the film surface near the crack edge downward while the further stress releasing near the crack edge dominated by local bending results in out-of-plane lifting. Actually, the analogous phenomenon is also obtained in previous work both by experimental observation and numerical simulation [52]. When the film thickness increases, the stress energy increases accordingly (for details see the following description), resulting in the increase of the crack width w, crack depth Δ, and lifting height δ.

It is well known that the internal stress is composed of intrinsic stress and thermal stress. For many film materials, the intrinsic growth stress is initially compressive, then tensile and then again compressive as the film thickness increases [65]. The residual stress in the film is further modified by thermal expansion mismatch during heating or cooling. In our experiment, the system temperature can increase obviously during deposition owing to the particle bombardment and heat radiation [53,56–59]. The average temperature of the film-substrate system can rise ~2.2 K/min during the film deposition measuring by an infrared thermometer. The thermal stress of the film can be calculated by $\sigma_{\text{th}} = \frac{E_f(\alpha_s-\alpha_f)\Delta T}{1-\nu_f}$, where E_f is the elastic modulus of film, ν_f is the Poisson's ratio of film, α_f is the thermal expansion coefficient of film, α_s is the thermal expansion coefficient of substrate, and ΔT is the temperature variation [65]. For Ni/PDMS system, $E_f \approx 200$ GPa, $\nu_f \approx 0.3$, $\alpha_f \approx 9 \times 10^{-6}\,\text{K}^{-1}$, $\alpha_s \approx 3.2 \times 10^{-4}\,\text{K}^{-1}$, $\Delta T \approx 44$ K for 20 min deposition, and then the thermal stress of the thickest film can be estimated to be about 4.0 GPa.

The stress energy increases with increasing deposition time, i.e., film thickness. When the tensile stress is beyond the breaking strength of the brittle Ni film, cracks start to form in the film. The selection of the cracking modes is mainly determined by the interfacial adhesion strength and substrate rigidity [22,23]. In our experiment, the energy of the sputtering particles is very large (about several electron-volts), improving the interfacial adhesion strength greatly [53,58,59]. As a result, the interface debonding and interface sliding are suppressed effectively. On the other hand, the PDMS substrate is soft compared to a rigid substrate, and thus the film crack can penetrate into the substrate easily [51–53]. Therefore, the cracks penetrating into the substrate are the most frequently observed mode in our experiment.

As shown in Fig. 1, a stable primary crack network has formed at about $h = 15$ nm. When the film thickness further increases, there are two mechanisms to release the increasing stress energy: enlarging the already existed cracks or forming new intersectional cracks. The former is favorable for weak interfacial adhesion cases such as the tectonic plates in geography or thin films floating on a liquid surface [66]. While the latter is favorable for strong interfacial adhesion cases such as the ceramic paints or thin films deposited on a rigid substrate [1,67]. In our experiment, the substrate is soft elastic PDMS, falling in between the liquid substrate and rigid substrate. As shown in Figs. 1 and 2, the stress energy is mainly released by enlarging the already existed cracks. Therefore, the primary crack number is almost unchanged but the crack width increases obviously with increasing film thickness.

B. Secondary cracks

Our experiment also shows that the film pieces surrounding by the primary cracks can further fracture to form fine crack networks (namely secondary cracking), as shown in Figs. 5(a) and 5(b). The secondary cracks are usually observed in the samples with larger film thickness ($h \geqslant 150$ nm). It can be seen from Fig. 2(d) that as the film thickness increases, the primary crack width increases quickly first and then the growth speed slows down gradually. It means that the residual tensile stress stored in the film pieces may increase with increasing film thickness. Therefore, the samples with larger film thickness are susceptible to generating secondary cracking. It should be noted here that the film pieces surrounding by the primary cracks are metastable although they are suffered from a large residual tensile stress. The spontaneous secondary cracks are randomly distributed in the film pieces for each sample.

The secondary cracks are quite different from the primary cracks and their differences are listed as following. First, the

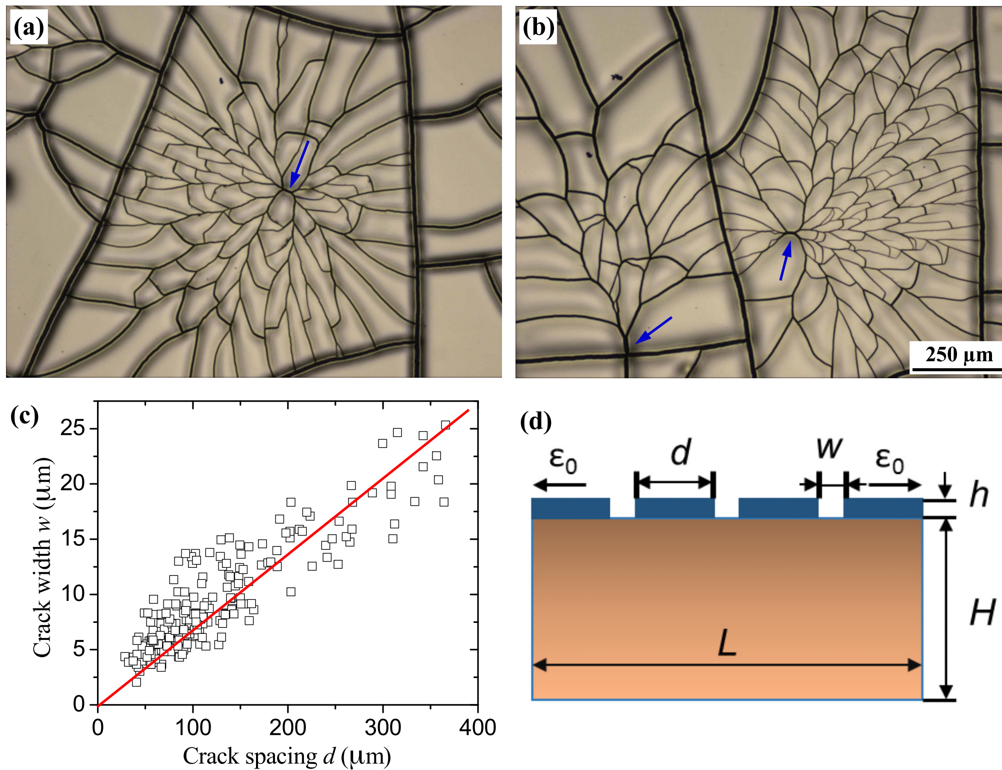

FIG. 5. (a), (b) Spontaneous crack branching phenomenon (secondary cracking) in the film pieces dividing by the primary cracks. The arrows denote the central points of crack nucleation. Each image has a size of $1390 \times 1040\,\mu\mathrm{m}^2$. $h = 150\,\mathrm{nm}$. (c) Dependence of the crack width w on the crack spacing d for the secondary cracking mode. The solid line is a linear fit to the experimental data. (d) Schematic diagram of secondary cracks in the film-substrate system. The symbols L, d, w, h, H, and ε_0 represent the substrate length, film island width, crack width, film thickness, substrate thickness, and tensile strain, respectively.

morphologies for primary and secondary cracks are different. The primary cracks are broad but their spacing is quite large, while the secondary cracks are narrow but dense. Usually, the larger crack spacing corresponds to a larger crack width. Figure 5(c) shows the quantitative relationship between the crack width w and the crack spacing d for the secondary cracking mode. It shows that the crack width w increases approximately linearly with the crack spacing d. The intersection angles of primary and secondary cracks are also quite different. The distributions of the intersection angles for primary and secondary cracks are shown in Supplemental Material Fig. S13 [55]. It shows that the angles between the primary cracks are close to 90 degrees, corresponding to the orthometric phenomenon of the primary cracks. However, the angles between the secondary cracks are deviated from 90 degrees greatly and the mean value is about 52 degrees.

Second, the formation processes of primary and secondary cracks are different. The primary cracks grow slowly and gradually during the film deposition while the secondary cracks propagate drastically and suddenly. The detailed structures for the primary and secondary cracks have been detected by the SEM, as shown in Fig. 6. The optical micrographs of the primary cracks with different magnifications are shown in Supplemental Material Fig. S10 [55]. It is clear that the secondary crack profile is comparatively smooth but the primary crack profile is much rough and step-like, indicating that the enlargement of the primary crack is not successive but step-by-step. During the film deposition, the tensile stress increases gradually. The energy releasing rate for a crack is proportional to the square of the tensile stress. When the energy releasing rate is larger than the relevant fracture resistance, the primary crack initiates and expands to a certain width instantaneously. After that, the local stress energy is released effectively and the crack expansion stops. Then the metal atoms deposit on the film pieces and the crack regions simultaneously, leading to the formation of a new continuous film with small thickness in the crack groove. Meanwhile, the tensile stress increases gradually and reaches the critical value again. Because the stress tends to concentrate at film imperfections and the thinner film possesses smaller breaking strength, the next cracking always occurs in the crack region, leading to the incremental expansion of the primary crack. Therefore, the primary crack profile is rough and step-like, showing multiple cracking traces. For secondary cracking mode, the crack formation is within a very short time, and thus the profile is comparatively smooth. It should be noted here that the secondary cracks can form during or after the film deposition. If the secondary cracks form during deposition, then the subsequently deposited film in the crack groove can undergo similar incremental expansion, leading to the increase of the width of the secondary cracks, as shown in Supplemental Material Fig. S14 [55].

Third, the driving factors for primary and secondary cracks are different. The primary cracks are driven by the thermal

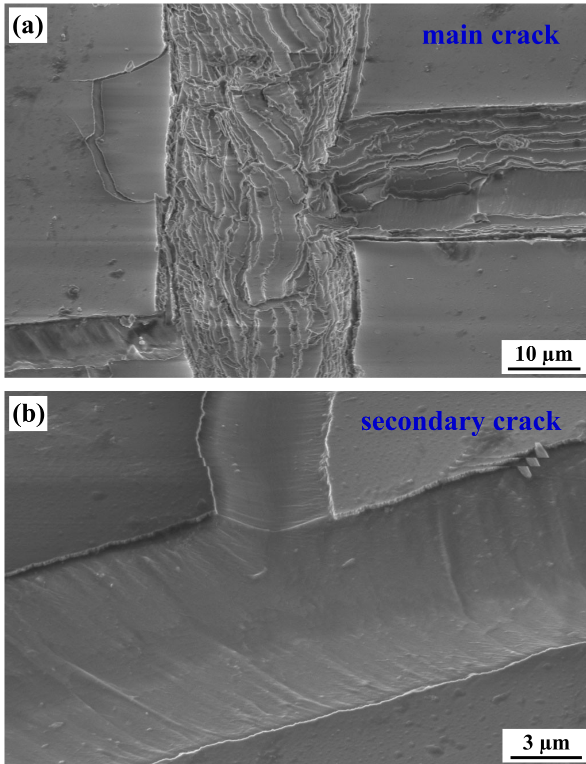

FIG. 6. Scanning electron microscopy (SEM) images for the primary (a) and secondary (b) cracks. $h = 150$ nm.

stress due to the temperature change during deposition, while the secondary cracks are mainly triggered by an external disturbance. As shown in Figs. 5(a) and 5(b), each secondary crack pattern possesses a central point, corresponding to the stress concentration and crack nucleation. Based on the experimental observations, the central points are randomly distributed on the film piece. They may be at the primary crack [Fig. 5(b), left], near the primary crack edge [Fig. 5(b), right], or close to the center of the film piece [Fig. 5(a)]. The secondary cracks propagate outwards from this central point, mainly along the radial direction with many bifurcations. During this process, triple-branched phenomena are frequently observed, and thus the angles between the secondary cracks are deviated from 90 degrees greatly. Similar branching phenomena of cracks can be observed in ceramics and glass plates shocked by heating or mechanical loading [68]. Due to the fact that the stress in a homogeneous film is uniform or equibiaxial, some crack segments along circumferential direction between the radial cracks can also be observed. Near the primary crack edges, the secondary cracks are all perpendicular to the primary cracks due to the free edge effect [1,4,52,53].

The secondary cracks shown in Fig. 5 are spontaneously formed when the sample was taken from the vacuum chamber. The driving factor for this pattern is not very clear, probably is due to the atmosphere pressure, film imperfection, external impact, etc. To artificially generate the secondary crack pattern, an un-cracked film piece was broken by a sharp pin. The surface morphologies of the film piece before and after breaking are shown in Fig. 7. It is clear that the artificial cracks are similar to the spontaneous secondary cracks shown in Fig. 5, although the crack number in Fig. 7 is much smaller. Figure 8 shows the secondary cracks triggered by an indentation with varied loads. We find that when the load P increases, the destroyed region at the indenter center enlarges gradually. The indentation-induced cracks are quite similar to the star-shaped crack pattern of broken windows when they are impacted locally [20]. The number of radial cracks increases with increasing load P, in agreement with the previous studies [20]. Again, all the radial cracks connect with the primary cracks perpendicularly due to the free edge effect [1,4,52,53]. Although the external loading can generate secondary cracking, the morphological characteristics and physical mechanisms of the spontaneous and indentation-induced cracks are different. First, the ambient environments are different. The spontaneous secondary cracks form during or after film deposition, perhaps in the vacuum condition, while the indentation-induced secondary cracks form in the atmosphere condition. Second, the film stresses are different. The indentation will introduce an additional stress field in the film. The additional stress is anisotropic and position-dependent, leading to a more complex stress distribution in the film piece.

C. Theoretical analysis

The relationship between the crack spacing and film thickness in film-substrate systems has been studied when the crack is confined to the film, which reveals that crack spacing would increase with increasing film thickness to minimize the total elastic energy [23,39,69]. In this experiment it shows that the crack depth Δ is in several micrometer range and the crack spacing d is in the range of several hundreds of micrometers. By contrast, the thickness of nickel film h is no more than 300 nm, which is far less than the crack spatial scales. So the observed cracks apparently penetrate from the film into the substrate. The cracks in the film are capable of penetrating into the substrate which is possible when the substrate is very soft. The optimal crack spacing is assumed to be the value of d that maximizes the energy releasing rate of the film-substrate system given the values of crack depth Δ, the residual tensile strain ε_0, the film thickness and other parameters of the film and substrate. According to the analysis for the cracking pattern of penetrated periodic crack array of films on soft substrates [54], the relationship between the average crack spacing d and the film thickness h is usually very complex as described in Eq. (1). It is only obtained numerically [54]:

$$\frac{d}{h} = f\left(\alpha, \beta, \frac{\varepsilon_0^2 \overline{E}_f h}{\Gamma_f}, \frac{\Gamma_f}{\Gamma_s}, \frac{H}{h}\right), \qquad (1)$$

where $\alpha = \frac{\overline{E}_f - \overline{E}_s}{\overline{E}_f + \overline{E}_s}$ and $\beta = \frac{\overline{E}_f(1-\nu_f)(1-2\nu_s) - \overline{E}_s(1-\nu_s)(1-2\nu_f)}{2(1-\nu_f)(1-\nu_s)(\overline{E}_f + \overline{E}_s)}$ are the Dundurs parameters of film and substrate system, $\overline{E} = E/(1-\upsilon^2)$ with $\{E_f, \upsilon_f\}$ and $\{E_s, \upsilon_s\}$ are the Young's modulus and Poisson's ratio of the film and substrate, respectively. $\{\Gamma_f, h\}$ and $\{\Gamma_s, H\}$ are the fracture toughness and thickness of film and substrate, respectively. In one limit case of cracks

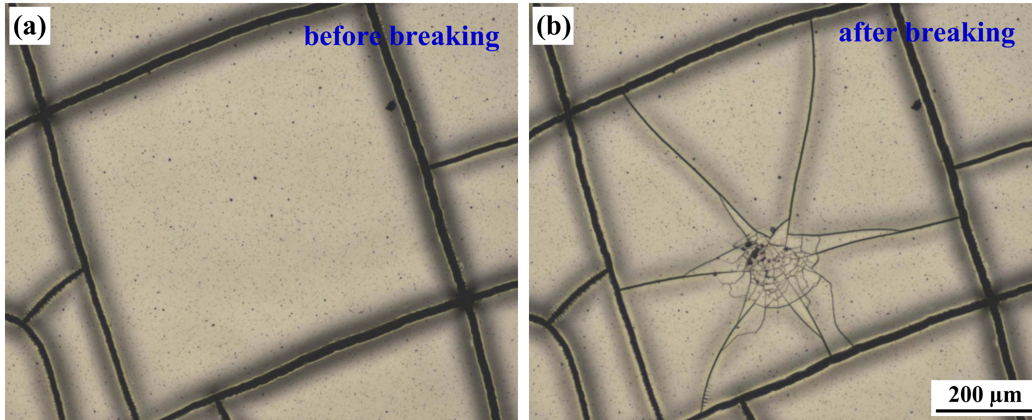

FIG. 7. Secondary cracking phenomenon of the Ni film triggered by a sharp pin. (a) Before breaking and (b) after breaking. Each image has a size of $1080 \times 880\,\mu\text{m}^2$. $h = 150\,\text{nm}$.

confined in the film, such as channel cracks with or without delamination, the optimal crack spacing is linearly dependent on the film thickness. Equation (1) has the form [54]

$$\frac{d}{h} = 5.6\left(\frac{\varepsilon_0^2 \overline{E}_f h}{\Gamma_f}\right)^{-1/2}. \tag{2}$$

In the case of channel crack $\varepsilon_0^2 \propto h^{-1}$, Eq. (2) thus recovers the power law of $d \propto h$. It is consistent with the common feature derived from shear-lag model [39,40] or the energy balance for Griffith cracks [26]. In the other limit case of cracks penetrating into an infinitely soft substrate, it is close to cracking in a free-standing film. The optimal crack spacing is determined by the energy balance between the elastic energy releasing rate in the film $\varepsilon_0^2 \overline{E}_f h d^2$ and the crack resistance of the film $\Gamma_f h d$. The resultant crack spacing is found to be insensitive to the film thickness but decreases with the increase of residual strain. In our experiments, the primary cracks caused by the high tensile stress in the film during the sputtering process penetrate into the PDMS soft substrate deeply. Their width and depth increase with increasing film thickness, while the number density is almost unchanged during deposition, in good agreement with our estimation. From the inset of Fig. 2(c) one can see that the normalized spacing monotonously decreases with the increase of film thickness, which is consistent with the numerical calculation result in a previous study [54].

When the crack patterns have formed in the film-substrate system, the crack width w is mainly balanced by the toughness of substrate. For simplicity, the crack penetrated into substrate is regarded as the mode I opening crack at the edge of an infinite semi-plane with the stress intensity factor $K_I \propto \sigma\sqrt{\pi\Delta}$, where σ is the stress in the substrate and Δ is the crack depth. Besides, according fracture mechanics the opening displacement r of the mode I crack is $r(y) = \frac{8K_I}{E}\sqrt{\frac{y}{2\pi}}$ with y the perpendicular distance from crack tip [see the profile in Fig. 3(a)]. Then one can see that the crack width at the surface

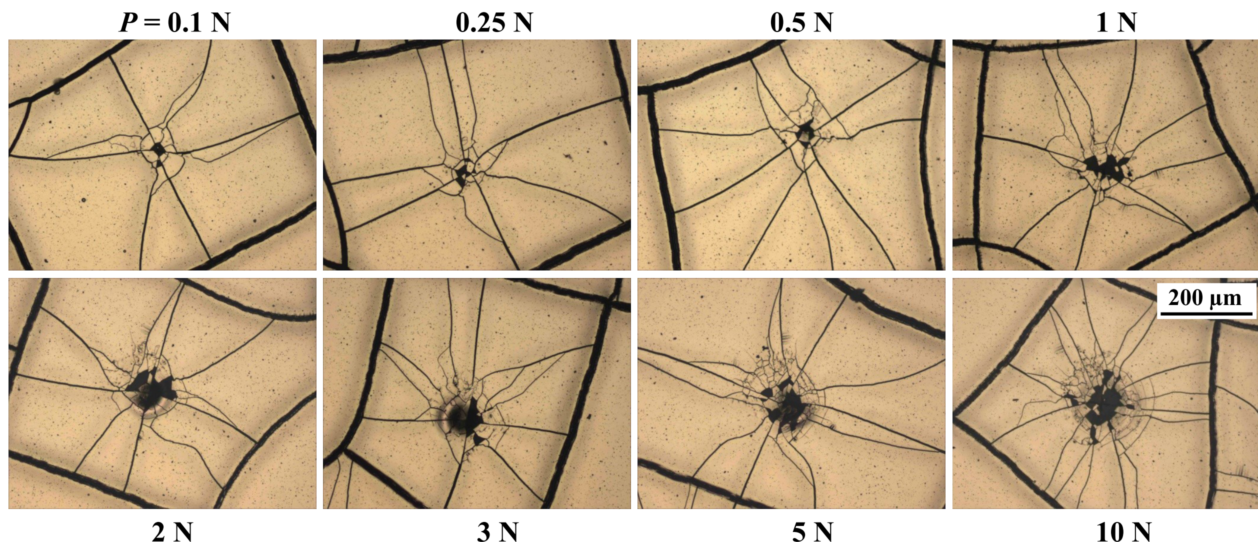

FIG. 8. Morphological evolution of the secondary cracks triggered by an indentation with varied loads P. Each image has a size of $695 \times 520\,\mu\text{m}^2$. $h = 150\,\text{nm}$.

of substrate $w = r(\Delta)$ is proportional to the crack depth $w \propto \Delta$, which is in a good agreement with the experiment result as shown in Fig. 4(a). Meanwhile, because the film stress σ is proportional to the film thickness h, the crack width w also has an approximately linear relationship with film thickness $w \propto h$, in agreement with the experimental result as shown in Fig. 2(d).

The secondary cracks in Figs. 5–8 present radial crack patterns and are perpendicular to the boundaries formed by the primary cracks. It can be interpreted that the tensile stress has been greatly released after the primary cracks form and the film stress that perpendicular to the boundaries has been released more by primary cracks. Then the stress paralleled to boundaries generates these radial secondary cracks. Figure 6(b) shows that the crack width of secondary crack is much larger than its depth. Penetration of the secondary cracks into the substrate is limited due to the tensile stress release by the primary cracks. Then to investigate the statistic result in Fig. 5(c) on the relationship between crack width and crack spacing, the cracked film-substrate system can be simplified as a soft substrate covered by film islands as shown in Fig. 5(d). We assume that there are N (N is relatively large so $N/(N+1) \approx 1$) islands on the substrate of length L, the length variation due to tensile stress of system with and without covered film islands are defined as Δd and Δw, and the corresponding strains are $\varepsilon_1 = \Delta d/d$ and $\varepsilon_2 = \Delta w/w$, respectively. Then the geometric constraints are $L = N(d+w)$, $\Delta L = N(\Delta d + \Delta w)$, and $\varepsilon_{\text{tot}} = \varepsilon_1 + \varepsilon_2$, where $\varepsilon_{\text{tot}} = \Delta L/L$ is the total strain. In this simplified model the force for different zones in substrate is the same so the strains ε_1 and ε_2 satisfy $\varepsilon_2 H E_s = \varepsilon_1 (H E_s + h E_f)$. From the above assumptions we can obtain that

$$\frac{w}{d} = \frac{1-\xi}{\xi\eta - 1}, \tag{3}$$

where $\xi = \varepsilon_1/\varepsilon_{\text{tot}}$ and $\eta = (HE_s + hE_f)/HE_s$. The strain ε_1 is equal to the critical fracture strain of the nickel film $\varepsilon_{\text{crack}}$, so ξ and η are both constants for the given cracked film-substrate system. Thus, Eq. (3) qualitatively reveals that the crack width w has a linear relationship with the crack spacing d, which can be also verified by the experimental observation in Fig. 5(c).

IV. CONCLUSIONS

In summary, metal nickel films have been sputter deposited on soft PDMS substrates and the cracking behaviors are described and discussed in detail. Two cracking modes, i.e., primary and secondary cracks, can be observed in the experiment. The morphological characteristics, growth behaviors, and formation mechanisms of these two cracking modes are quite different. The primary cracks are driven by the thermal stress during deposition and they can penetrate into the PDMS substrate deeply. Their expansion is slow and step-by-step. Therefore, the primary cracks grow sequentially and the subsequent cracks usually meets the existing cracks at T-shaped junctions. The width and depth of the primary cracks both increase with increasing film thickness, while the spacing is insensitive to the film thickness, totally different from that of the previous mud crack patterns. The secondary cracks are triggered by the external disturbance in the presence of the primary cracks and they seldom penetrate into the substrate due to the limit energy releasing rate. Their formation is within a very short time and they are narrow but dense. The width of secondary cracks is inversely proportional to the crack number density. The different geometric features of both primary and secondary cracks observed in experiment are in good agreement with the theoretical predictions based on the principle of fracture mechanics. The report in this work will provide a deep insight into the cracking behaviors of brittle films on soft elastic substrates. Furthermore, the experimental technique can be developed to generate complex hierarchical crack patterns, which may be beneficial for technique applications such as pressure sensors, templates, biomimics, and surface engineering.

ACKNOWLEDGMENTS

This work was supported by the National Natural Science Foundation of China (Grants No. 11204283, No. 11104054, No. 11472262, and No. 11672285) and the Strategic Priority Research Program of the Chinese Academy of Sciences (Grant No. XDB22040502), the Collaborative Innovation Center of Suzhou Nano Science and Technology, and the Fundamental Research Funds for the Central Universities (Grant No. WK2090050043).

[1] L. Goehring, A. Nakahara, T. Dutta, S. Tarafdar, and S. Kitsunezaki, *Desiccation Cracks and Their Patterns: Formation and Modelling in Science and Nature* (John Wiley & Sons, New York, 2015).

[2] L. Goehring and S. W. Morris, Phys. Today **67**, 39 (2014).

[3] M. C. Milinkovitch, L. Manukyan, A. Debry, N. Di-Poï, S. Martin, D. Singh, D. Lambert, and M. Zwicker, Science **339**, 78 (2013).

[4] S. Yu, X. Zhang, X. Xiao, H. Zhou, and M. Chen, Soft Matter **11**, 2203 (2015).

[5] P. H. Ho, Y. T. Liou, C. H. Chuang, S. W. Lin, C. Y. Tseng, D. Y. Wang, C. C. Chen, W. Y. Hung, C. Y. Wen, and C. W. Chen, Adv. Mater. **27**, 1724 (2015).

[6] Z. Néda, K.-t. Leung, L. Józsa, and M. Ravasz, Phys. Rev. Lett. **88**, 095502 (2002).

[7] D. Huh, K. L. Mills, X. Zhu, M. A. Burns, M. D. houless, and S. Takayama, Nat. Mater. **6**, 424 (2007).

[8] M. Kim, D. Ha, and T. Kim, Nat. Commun. **6**, 6247 (2015).

[9] A. Chortos, J. Lim, J. W. To, M. Vosgueritchian, T. J. Dusseault, T. H. Kim, S. Hwang, and Z. Bao, Adv. Mater. **26**, 4253 (2014).

[10] K. D. M. Rao, R. Gupta, and G. U. Kulkarni, Adv. Mater. Interfaces **1**, 1400090 (2014).

[11] B. Han, K. Pei, Y. Huang, X. Zhang, Q. Rong, Q. Lin, Y. Guo, T. Sun, C. Guo, D. Carnahan, M. Giersig, Y. Wang, J. Gao, Z. Ren, and K. Kempa, Adv. Mater. **26**, 873 (2014).

[12] D. Kang, P. V. Pikhitsa, Y. W. Choi, C. Lee, S. S. Shin, L. Piao, B. Park, K. Y. Suh, T. Kim, and M. Choi, Nature **516**, 222 (2014).
[13] B. Sarkar, D. K. Satapathy, and M. Jaiswal, Nanoscale **11**, 200 (2019).
[14] Q. Zhuang, S. C. Warren, B. Baytekin, A. F. Demirörs, P. P. Pillai, B. Kowalczyk, H. T. Baytekin, and B. Grzybowski, Adv. Mater. **26**, 3667 (2014).
[15] Y. Han, Y. Liu, W. Wang, J. Leng, and P. Jin, Soft Matter **12**, 2708 (2016).
[16] X. Zhu, K. L. Mills, P. R. Peters, J. H. Bahng, E. H. Liu, J. Shim, K. Naruse, M. E. Csete, M. D. Thouless, and S. Takayama, Nat. Mater. **4**, 403 (2005).
[17] K. H. Nam, I. H. Park, and S. H. Ko, Nature **485**, 221 (2012).
[18] A. Yuse and M. Sano, Nature **362**, 329 (1993).
[19] J. F. Fuentealba, E. Hamm, and B. Roman, Phys. Rev. Lett. **116**, 165501 (2016).
[20] N. Vandenberghe, R. Vermorel, and E. Villermaux, Phys. Rev. Lett. **110**, 174302 (2013).
[21] M. É. Schwaab, T. Biben, S. Santucci, A. Gravouil, and L. Vanel, Phys. Rev. Lett. **120**, 255501 (2018).
[22] J. W. Hutchinson and Z. Suo, Adv. Appl. Mech. **29**, 63 (1991).
[23] M. D. Thouless, Thin Solid Films **181**, 397 (1989).
[24] Z. C. Xia and J. W. Hutchinson, J. Mech. Phys. Solids **48**, 1107 (2000).
[25] J. Zhang, Y. Lu, L. He, L. Yang, and Y. Ni, Eng. Fract. Mech. **177**, 123 (2017).
[26] J. Marthelot, B. Roman, J. Bico, J. Teisseire, D. Dalmas, and F. Melo, Phys. Rev. Lett. **113**, 085502 (2014).
[27] P. Bacchin, D. Brutin, A. Davaille, E. Di Giuseppe, X. D. Chen, I. Gergianakis, F. Giorgiutti-Dauphiné, L. Goehring, Y. Hallez, R. Heyd, and R. Jeantet, Eur. Phys. J. E **41**, 94 (2018).
[28] R. Seghir and S. Arscott, Sci. Rep. **5**, 14787 (2015).
[29] M. Gao, X. Huang, and Y. Zhao, Sci. China Technol. Sci. **61**, 949 (2018).
[30] V. Lazarus and L. Pauchard, Soft Matter **7**, 2552 (2011).
[31] J. Li, A. K. Dozier, Y. Li, F. Yang, and Y. T. Cheng, J. Electrochem. Soc. **158**, A689 (2011).
[32] S. Bohn, L. Pauchard, and Y. Couder, Phys. Rev. E **71**, 046214 (2005).
[33] S. Bohn, J. Platkiewicz, B. Andreotti, M. Adda-Bedia, and Y. Couder, Phys. Rev. E **71**, 046215 (2005).
[34] S. Bohn, S. Douady, and Y. Couder, Phys. Rev. Lett. **94**, 054503 (2005).
[35] M. Hofmann, R. Anderssohn, H. A. Bahr, H. J. Weiß, and J. Nellesen, Phys. Rev. Lett. **115**, 154301 (2015).
[36] H. Yao, Z. Xie, C. He, and M. Dao, Sci. Rep. **5**, 8011 (2015).
[37] K. A. Shorlin, J. R. de Bruyn, M. Graham, and S. W. Morris, Phys. Rev. E **61**, 6950 (2000).
[38] T. S. Komatsu and S. I. Sasa, Jap. J. Appl. Phys. **36**, 391 (1997).
[39] M. D. Thouless, J. Am. Ceram. Soc. **73**, 2144 (1990).
[40] M. Yanaka, Y. Tsukahara, N. Nakaso, and N. Takeda, J. Mater. Sci. **33**, 2111 (1998).
[41] J. Marthelot, J. Bico, F. Melo, and B. Roman, J. Mech. Phys. Solids **84**, 214 (2015).
[42] X. Ma, J. Lowensohn, and J. C. Burton, Phys. Rev. E **99**, 012802 (2019).
[43] S. Kitsunezaki, Phys. Rev. E **60**, 6449 (1999).
[44] E. A. Jagla and A. G. Rojo, Phys. Rev. E **65**, 026203 (2002).
[45] J. C. Flores, Soft Matter **13**, 1352 (2017).
[46] V. Lazarus, Europhys. Lett. **117**, 24002 (2017).
[47] F. Giorgiutti-Dauphiné and L. Pauchard, J. Appl. Phys. **120**, 065107 (2016).
[48] R. G. Elliman, M. Spooner, T. D. M. Dall, T. H. Kim, and N. H. Fletcher, Philos. Mag. **87**, 4893 (2007).
[49] C. Ju, F. Xue, F. Huang, L. Q. Chen, X. Lu, J. Zhu, and H. M. Jensen, Appl. Phys. Lett. **106**, 201905 (2015).
[50] M. Kim, D. J. Kim, D. Ha, and T. Kim, Nanoscale **8**, 9461 (2016).
[51] T. Guo, L. Qiao, X. Pang, and A. A. Volinsky, Acta Mater. **99**, 273 (2015).
[52] N. J. Douville, Z. Li, S. Takayama, and M. D. Thouless, Soft Matter **7**, 6493 (2011).
[53] T. Ibru, K. Kalaitzidou, J. K. Baldwin, and A. Antoniou, Soft Matter **13**, 4035 (2017).
[54] M. D. Thouless, Z. Li, N. J. Douville, and S. Takayama, J. Mech. Phys. Solids **59**, 1927 (2011).
[55] See Supplemental Material at http://link.aps.org/supplemental/10.1103/PhysRevE.100.052804 for details about the wrinkle morphologies of thinner films before and after crack formation, crack morphologies and structural characteristics of both flat and thickness-gradient films, and cross-sectional profiles of the nickel/PDMS sample taken by optical microscopy and SEM. Fourteen supplemental figures are provided.
[56] S. Yu, Y. Ni, L. He, and Q. L. Ye, ACS Appl. Mater. Interfaces **7**, 5160 (2015).
[57] N. Bowden, S. Brittain, A. G. Evans, J. W. Hutchinson, and G. M. Whitesides, Nature **393**, 146 (1998).
[58] S. Yu, Y. Sun, S. Li, and Y. Ni, Soft Matter **14**, 6745 (2018).
[59] S. Yu, L. Ma, Y. Sun, C. Lu, H. Zhou, and Y. Ni, Langmuir **35**, 7146 (2019).
[60] J. Yin and X. Chen, Philos. Mag. Lett. **90**, 423 (2010).
[61] Y. Ni, D. Yang, and L. He, Phys. Rev. E **86**, 031604 (2012).
[62] M. Léang, F. Giorgiutti-Dauphiné, L. T. Lee, and L. Pauchard, Soft Matter **13**, 5802 (2017).
[63] M. George, C. Coupeau, J. Colin, and J. Grilhé, Thin solid films **429**, 267 (2003).
[64] A. Polywka, L. Stegers, O. Krauledat, T. Riedl, T. Jakob, and P. Görrn, Nanomaterials **6**, 168 (2016).
[65] L. B. Freund and S. Suresh, *Thin Film Materials: Stress, Defect Formation and Surface Evolution* (Cambridge University Press, Cambridge, UK, 2004).
[66] S. J. Yu and Y. J. Zhang, Surf. Rev. Lett. **15**, 525 (2008).
[67] H. N. Iben and J. F. O'brien, Graph. Models **71**, 198 (2009).
[68] W. Pompe, H. A. Bahr, I. Pflugbeil, G. Kirchhoff, P. Langmeier, and H. J. Weiss, Mater. Sci. Eng. A **233**, 167 (1997).
[69] V. B. Shenoy, A. F. Schwartzman, and L. B. Freund, Int. J. Fracture **109**, 29 (2001).